

# Journal of Electronic Imaging

JElectronicImaging.org

## Multimodal sparse reconstruction in guided wave imaging of defects in plates

Andrew Golato  
Sridhar Santhanam  
Fauzia Ahmad  
Moeness G. Amin

# Multimodal sparse reconstruction in guided wave imaging of defects in plates

Andrew Golato, Sridhar Santhanam, Fauzia Ahmad,\* and Moeness G. Amin

Villanova University, College of Engineering, Center for Advanced Communications, 800 East Lancaster Avenue, Villanova, Pennsylvania 19085, United States

**Abstract.** A multimodal sparse reconstruction approach is proposed for localizing defects in thin plates in Lamb wave-based structural health monitoring. The proposed approach exploits both the sparsity of the defects and the multimodal nature of Lamb wave propagation in plates. It takes into account the variation of the defects' aspect angles across the various transducer pairs. At low operating frequencies, only the fundamental symmetric and antisymmetric Lamb modes emanate from a transmitting transducer. Asymmetric defects scatter these modes and spawn additional converted fundamental modes. Propagation models are developed for each of these scattered and spawned modes arriving at the various receiving transducers. This enables the construction of modal dictionary matrices spanning a two-dimensional array of pixels representing potential defect locations in the region of interest. Reconstruction of the region of interest is achieved by inverting the resulting linear model using the group sparsity constraint, where the groups extend across the various transducer pairs and the different modes. The effectiveness of the proposed approach is established with finite-element scattering simulations of the fundamental Lamb wave modes by crack-like defects in a plate. The approach is subsequently validated with experimental results obtained from an aluminum plate with asymmetric defects. ©2016 SPIE and IS&T [DOI: 10.1117/1.JEI.25.4.043013]

Keywords: sparse reconstruction; multimodal; lamb waves; structural health monitoring.

Paper 16220P received Mar. 21, 2016; accepted for publication Jun. 30, 2016; published online Jul. 20, 2016.

## 1 Introduction

Structural health monitoring (SHM) is at the forefront of emerging methods for the assessment of the integrity of a variety of structures.<sup>1-4</sup> Under the realm of SHM applications, guided ultrasonic waves are employed for real-time detection and localization of defects in thin-walled structures, such as aircraft wings and wind turbine blades.<sup>5-8</sup> Guided ultrasonic waves in such structures are referred to as Lamb waves.<sup>9-11</sup> These waves are solutions to the wave equation for a thin plate, subject to traction free conditions on the plate surfaces. Lamb wave-based sensing modality has gained preference in SHM of thin plate and shell structures due to the ability of these waves to travel large distances without significant attenuation, while providing rich interactions with defects.<sup>12-15</sup> As such, Lamb wave-based SHM systems permit quick examination of broad areas of structures with a small number of transducers, thereby offering cost savings and economic advantages.

Much of the attention garnered lately by Lamb wave-based SHM is due to recent advances in computing, processing, and electronic technologies that can handle the complexities associated with Lamb wave propagation. Several factors contribute toward the complexity of Lamb wave-based SHM. Lamb wave propagation is multimodal in nature. The multiple modes can be separated into symmetric (S) and antisymmetric (A) modes. The total number of symmetric and antisymmetric modes present can be controlled by the choice of the frequency of operation. At low frequencies, only the fundamental symmetric ( $S_0$ ) and antisymmetric

( $A_0$ ) modes are present. However, at higher frequencies, there can be a profusion of higher order Lamb modes propagating in the thin structure. It is noted that at a given frequency, each mode propagates with a different speed. All modes are dispersive since the phase and group velocity of each individual mode is a function of frequency. The additional wave modes spawned by asymmetric defects are responsible for added complexity in the Lamb wave signal.<sup>16,17</sup>

The multimodal nature of Lamb waves has typically been considered a nuisance and avoided by operation at a sufficiently low frequency where only a single fundamental propagating mode exists. Despite the complexity of the propagating Lamb waves, the additional information contained in the various modes can be properly exploited to provide an enhanced assessment of the health of the structure. For instance, the antisymmetric modes,  $A_0$  and  $A_1$ , interact well with delamination cracks lying in a plane parallel to the plane of the plate. Meanwhile, the  $S_0$  mode is appropriate for detecting transverse cracks in the middle of thin plates, and the symmetric  $S_1$  mode is well suited for detecting smaller transverse cracks at the surface of plates.<sup>14,15,18</sup>

While several techniques exist, including delay-and-sum beamforming, adaptive beamforming, and sparse reconstruction,<sup>16,19-23</sup> for defect localization under single Lamb mode propagation, research efforts have only recently been directed toward exploiting the multimodal nature of Lamb waves in SHM. Subspace-based high-resolution methods were reported in Ref. 24. A data-driven improvement to matched field processing for defect localization in a

\*Address all correspondence: Fauzia Ahmad, E-mail: [fauzia.ahmad@villanova.edu](mailto:fauzia.ahmad@villanova.edu)

multimodal propagation environment was utilized in Ref. 25. Sparse signal recovery methods were employed in Ref. 26 to account for mode conversion under single-mode excitation in ultrasonic nondestructive evaluation applications, which can also be applied to address defect-spawned modes in Lamb wave-based SHM. In previous work, we have utilized sparse reconstruction for multimodal imaging in SHM.<sup>27,28</sup> The case of multiple modes emanating from the transmitters and being scattered by defects was considered in Ref. 27. This case was extended in Ref. 28 by the inclusion of additional defect-spawned modes. However, both Refs. 27 and 28 ignored the dependency of the defect scattering on the aspect angle and did not provide rigorous performance validation.

In this paper, we perform joint exploitation of the multimodal nature of the Lamb waves and the sparse nature of the defects for efficient and reliable defect localization using a limited number of transducers distributed around the region of interest (ROI). The received signal model considers both excited and defect-spawned  $S_0$  and  $A_0$  Lamb modes and accounts for the fact that the defects' aspect angles may vary considerably across the various transmitter–receiver transducer pairs. The defect localization problem is formulated as group sparse reconstruction, which exploits the multimodal measurements from all transducers to form an image of the ROI. Note that although only two excited fundamental modes are considered herein, the proposed model and reconstruction method can readily be extended to a higher number of Lamb wave modes. The effectiveness of the proposed method is verified through both finite-element simulations and real data experiments; the former involves symmetric crack-like defects in a plate, whereas the latter deals with a thin aluminum plate with masses glued to the surface to simulate asymmetric defects. To the best of our knowledge, multimodal exploitation in sparse image reconstruction for varying defects' aspect angles across the different transmitter–receiver pairs has not been addressed in prior works in the context of guided wave SHM.

The remainder of this paper is organized as follows. In Sec. 2, the multimodal signal model is formulated and the sparse reconstruction approach for defect localization is presented. Supporting finite-element simulation results are provided in Sec. 3, while experimental results are presented in Sec. 4, both of which demonstrate the efficacy of the multimodal sparse reconstruction approach in localizing defects in thin plate-like structures. Section 5 contains the concluding remarks.

## 2 Multimodal Signal Model and Sparse Reconstruction

In this section, we first present the multimodal signal model, followed by a description of the sparsity-based scene reconstruction for defect localization.

### 2.1 Signal Model

Consider a spatially distributed network of  $J$  piezoelectric transducers attached to one of the surfaces of a thin plate (as shown in Fig. 1). The transducers are assumed to be employed in a pitch-catch mode for data collection. That is, the transducers work in pairs with one transducer transmitting the signal and the other acting as the receiver. As

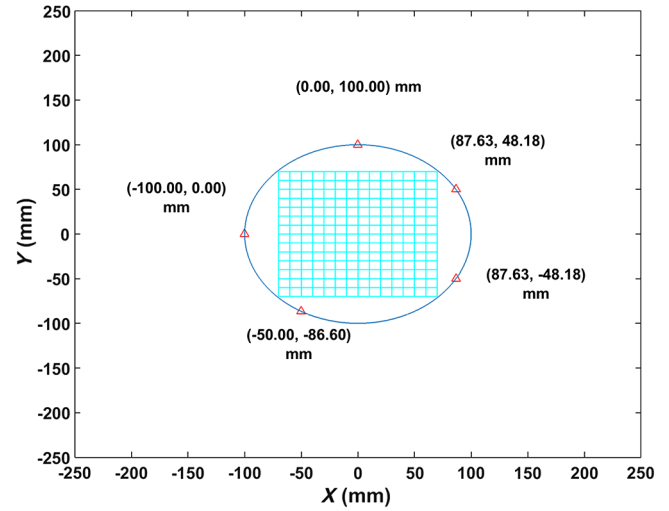


**Fig. 1** Simulation setup (top view). The cyan grid indicates the ROI and the red triangles represent the transducers located circumferentially around the blue circle of radius 100 mm.

such, a total of  $L = J(J - 1)/2$  unique transmitter–receiver combinations are used for interrogating the ROI.

Let the transmitter and receiver corresponding to the  $l$ 'th pair be located at position vectors  $\mathbf{t}_l$  and  $\mathbf{r}_l$ , respectively. Let  $h(t)$  be the analytic signal corresponding to the excitation waveform, whose center frequency is chosen such that the only modes propagating in the plate are the fundamental  $A_0$  and  $S_0$  modes. For a single defect located at position vector  $\mathbf{s}_p$ , both  $S_0$  and  $A_0$  waves will be scattered by the defect. The respective received scattered waves at  $\mathbf{r}_l$  for the two modes can be expressed in the frequency domain as

$$G_{lp,A_0}(f) = \left( \frac{\alpha}{\|\mathbf{t}_l - \mathbf{s}_p\|_2} \right)^{0.5} \left( \frac{\alpha}{\|\mathbf{r}_l - \mathbf{s}_p\|_2} \right)^{0.5} \sigma_{lp,A_0} H(f) \times \exp[j2\pi f(\|\mathbf{t}_l - \mathbf{s}_p\|_2 + \|\mathbf{r}_l - \mathbf{s}_p\|_2)/c_{A_0}(f)], \quad (1)$$

$$G_{lp,S_0}(f) = \left( \frac{\alpha}{\|\mathbf{t}_l - \mathbf{s}_p\|_2} \right)^{0.5} \left( \frac{\alpha}{\|\mathbf{r}_l - \mathbf{s}_p\|_2} \right)^{0.5} \sigma_{lp,S_0} H(f) \times \exp[j2\pi f(\|\mathbf{t}_l - \mathbf{s}_p\|_2 + \|\mathbf{r}_l - \mathbf{s}_p\|_2)/c_{S_0}(f)], \quad (2)$$

where  $H(f)$  is the Fourier transform of  $h(t)$ ,  $c_{A_0}$ , and  $c_{S_0}$  are the frequency-dependent phase speeds of the  $A_0$  and  $S_0$  modes, respectively, and  $\alpha$  is an arbitrary constant with dimensions of length. The inverse square root dependence on  $\|\mathbf{t}_l - \mathbf{s}_p\|_2$  and  $\|\mathbf{r}_l - \mathbf{s}_p\|_2$  accounts for attenuation caused by the geometrical spreading of the wavefront on the transmit and receive paths to the defect. The parameters  $\sigma_{lp,A_0}$  and  $\sigma_{lp,S_0}$  are the respective defect reflectivities under the  $A_0$  and  $S_0$  modes. While the reflectivities are assumed to be independent of frequency, they are functions of the aspect angles relative to the  $l$ 'th transmitter–receiver pair.

In addition to these scattered modes, an incident  $A_0$  mode, upon interaction with an asymmetric defect, will spawn an additional  $S_0$  mode, where the asymmetry of the defect is defined relative to the midplane of the plate. The same

phenomenon occurs for the  $S_0$  mode interacting with the asymmetric defect, resulting in an additional spawned  $A_0$  mode. The received signal components corresponding to these two converted modes are represented in the frequency domain as

$$G_{I_p, A_0/S_0}(f) = \left( \frac{\alpha}{\|\mathbf{t}_l - \mathbf{s}_p\|_2} \right)^{0.5} \left( \frac{\alpha}{\|\mathbf{r}_l - \mathbf{s}_p\|_2} \right)^{0.5} \sigma_{I_p, A_0/S_0} H(f) \times \exp \left[ j2\pi f \left( \frac{\|\mathbf{t}_l - \mathbf{s}_p\|_2}{c_{A_0}(f)} + \frac{\|\mathbf{r}_l - \mathbf{s}_p\|_2}{c_{S_0}(f)} \right) \right], \quad (3)$$

$$G_{I_p, S_0/A_0}(f) = \left( \frac{\alpha}{\|\mathbf{t}_l - \mathbf{s}_p\|_2} \right)^{0.5} \left( \frac{\alpha}{\|\mathbf{r}_l - \mathbf{s}_p\|_2} \right)^{0.5} \sigma_{I_p, S_0/A_0} H(f) \times \exp \left[ j2\pi f \left( \frac{\|\mathbf{t}_l - \mathbf{s}_p\|_2}{c_{S_0}(f)} + \frac{\|\mathbf{r}_l - \mathbf{s}_p\|_2}{c_{A_0}(f)} \right) \right], \quad (4)$$

where the notation  $S_0/A_0$  and  $A_0/S_0$  denote the two converted modes with reflectivities  $\sigma_{I_p, A_0/S_0}$  and  $\sigma_{I_p, S_0/A_0}$ ; i.e., the incident  $S_0$  wave that spawns a reflected  $A_0$  from the defect and vice versa. For convenience, the attenuation factors in Eqs. (1)–(4) can be combined with the respective defect reflectivities, leading to

$$G_{I_p, A_0}(f) = x_{I_p, A_0} H(f) \exp[j2\pi f (\|\mathbf{t}_l - \mathbf{s}_p\|_2 + \|\mathbf{r}_l - \mathbf{s}_p\|_2) / c_{A_0}(f)], \quad (5)$$

$$G_{I_p, S_0}(f) = x_{I_p, S_0} H(f) \exp[j2\pi f (\|\mathbf{t}_l - \mathbf{s}_p\|_2 + \|\mathbf{r}_l - \mathbf{s}_p\|_2) / c_{S_0}(f)], \quad (6)$$

$$G_{I_p, A_0/S_0}(f) = x_{I_p, A_0/S_0} H(f) \times \exp \left[ j2\pi f \left( \frac{\|\mathbf{t}_l - \mathbf{s}_p\|_2}{c_{A_0}(f)} + \frac{\|\mathbf{r}_l - \mathbf{s}_p\|_2}{c_{S_0}(f)} \right) \right], \quad (7)$$

$$G_{I_p, S_0/A_0}(f) = x_{I_p, S_0/A_0} H(f) \times \exp \left[ j2\pi f \left( \frac{\|\mathbf{t}_l - \mathbf{s}_p\|_2}{c_{S_0}(f)} + \frac{\|\mathbf{r}_l - \mathbf{s}_p\|_2}{c_{A_0}(f)} \right) \right]. \quad (8)$$

The time-domain equivalents of the received signal components corresponding to the direct and converted modes are simply the inverse Fourier transforms of Eqs. (5)–(8) and are denoted by  $g_{I_p, A_0}(t)$ ,  $g_{I_p, S_0}(t)$ ,  $g_{I_p, A_0/S_0}(t)$ , and  $g_{I_p, S_0/A_0}(t)$ , respectively. Thus, the total received signal at  $\mathbf{r}_l$  due to the defect at  $\mathbf{s}_p$  is given as

$$\tilde{z}_l(t) = b_l(t) + g_{I_p, A_0}(t) + g_{I_p, S_0}(t) + g_{I_p, A_0/S_0}(t) + g_{I_p, S_0/A_0}(t), \quad (9)$$

where  $b_l(t)$  represents the background signal corresponding to the  $l$ 'th transmitter–receiver pair, which comprises the direct path signals between the transmitter and receiver as well as any edge reflections.

For the general case of  $P$  structural defects in the plate, the received signal, pertaining to the  $l$ 'th transmitter–receiver pair, is obtained by the superposition of the direct signal

and the complete set of scattered and converted modes produced by all defects and is expressed as

$$\tilde{z}_l(t) = b_l(t) + \sum_{p=0}^{P-1} [g_{I_p, A_0}(t) + g_{I_p, S_0}(t) + g_{I_p, A_0/S_0}(t) + g_{I_p, S_0/A_0}(t)]. \quad (10)$$

Note that the interactions between the defects are ignored in this model. Further, access to the background signals in the absence of the defects is assumed. This permits background subtraction to be performed, resulting in a difference signal, which only contains the defect-scattered and defect-spawned waveforms

$$z_l(t) = \tilde{z}_l(t) - b_l(t) = \sum_{p=0}^{P-1} [g_{I_p, A_0}(t) + g_{I_p, S_0}(t) + g_{I_p, A_0/S_0}(t) + g_{I_p, S_0/A_0}(t)]. \quad (11)$$

## 2.2 Matrix–Vector Representation

An equivalent matrix–vector representation of the difference signals,  $z_l(t)$ ,  $l = 0, 1, \dots, L-1$ , is obtained as follows. The ROI is conceptualized as a uniform grid of  $M$  pixels where each pixel represents a potential defect location. In general,  $P \ll M$ , i.e., the number of defects is typically much smaller than the number of potential defect locations. Let  $\mathbf{x}_{l, A_0}$  and  $\mathbf{x}_{l, S_0}$  be the lexicographically ordered  $M \times 1$  scene reflectivity vectors corresponding to the spatial sampling grid for the  $l$ 'th transmitter–receiver pair under the  $A_0$  and  $S_0$  modes, respectively. Likewise,  $\mathbf{x}_{l, A_0/S_0}$  and  $\mathbf{x}_{l, S_0/A_0}$  represent the respective scene reflectivity vectors under the converted modes of the incident  $A_0$  and  $S_0$  modes. Sampling  $z_l(t)$  at times  $t_k$ ,  $k = 0, 1, \dots, K-1$ , we obtain a  $K \times 1$  vector  $\mathbf{z}_l$ . Then, using Eqs. (5)–(8) and (11) and with the introduction of measurement noise  $\mathbf{n}_l$ , we obtain the linear relationship between the  $l$ 'th difference signal and the corresponding scene reflectivity vectors as

$$\mathbf{z}_l = \Psi_{l, A_0} \mathbf{x}_{l, A_0} + \Psi_{l, S_0} \mathbf{x}_{l, S_0} + \Psi_{l, A_0/S_0} \mathbf{x}_{l, A_0/S_0} + \Psi_{l, S_0/A_0} \mathbf{x}_{l, S_0/A_0} + \mathbf{n}_l, \quad (12)$$

where  $\Psi_{l, A_0}$ ,  $\Psi_{l, S_0}$ ,  $\Psi_{l, A_0/S_0}$ , and  $\Psi_{l, S_0/A_0}$  are the dictionary matrices corresponding to the scattered and the converted modes, each of dimension  $K \times M$ . The  $m$ 'th column of  $\Psi_{l, A_0}$  consists of the scattered  $A_0$  wave corresponding to a defect at the  $m$ 'th grid-point  $\mathbf{s}_m$  with the  $k$ 'th element of the  $m$ 'th column given as

$$(\Psi_{l, A_0})_{k, m} = F^{-1} \{ H(f) \exp[j2\pi f (\|\mathbf{t}_l - \mathbf{s}_m\|_2 + \|\mathbf{r}_l - \mathbf{s}_m\|_2) / c_{A_0}(f)] \} |_{t=t_k}, \quad (13)$$

where  $F^{-1}\{\cdot\}$  is the inverse Fourier Transform operator. Likewise, the  $m$ 'th column of  $\Psi_{l, S_0}$  consists of the scattered  $S_0$  wave corresponding to a defect at  $\mathbf{s}_m$  with its  $k$ 'th element given as

$$(\Psi_{l, S_0})_{k, m} = F^{-1} \{ H(f) \exp[j2\pi f (\|\mathbf{t}_l - \mathbf{s}_m\|_2 + \|\mathbf{r}_l - \mathbf{s}_m\|_2) / c_{S_0}(f)] \} |_{t=t_k}. \quad (14)$$

The same logic follows for the converted mode dictionary matrices, with the corresponding  $(k, m)$ 'th elements expressed as

$$(\Psi_{l,S_0/A_0})_{k,m} = F^{-1} \left\{ H(f) \exp \left[ j2\pi f \left( \frac{\|\mathbf{t}_l - \mathbf{s}_m\|_2}{c_{S_0}(f)} + \frac{\|\mathbf{r}_l - \mathbf{s}_m\|_2}{c_{A_0}(f)} \right) \right] \right\} \Big|_{t=t_k}, \quad (15)$$

$$(\Psi_{l,A_0/S_0})_{k,m} = F^{-1} \left\{ H(f) \exp \left[ j2\pi f \left( \frac{\|\mathbf{t}_l - \mathbf{s}_m\|_2}{c_{A_0}(f)} + \frac{\|\mathbf{r}_l - \mathbf{s}_m\|_2}{c_{S_0}(f)} \right) \right] \right\} \Big|_{t=t_k}. \quad (16)$$

Equation (12) only considers the contribution of a single transmitter–receiver pair. The signal model corresponding to all  $L$  transmitter–receiver combinations can be obtained as

$$\mathbf{z} = \Psi_{A_0} \mathbf{x}_{A_0} + \Psi_{S_0} \mathbf{x}_{S_0} + \Psi_{A_0/S_0} \mathbf{x}_{A_0/S_0} + \Psi_{S_0/A_0} \mathbf{x}_{S_0/A_0} + \mathbf{n}, \quad (17)$$

where

$$\begin{aligned} \mathbf{z} &= (\mathbf{z}_0^T \ \mathbf{z}_1^T \ \cdots \ \mathbf{z}_{L-1}^T)^T, \\ \mathbf{n} &= (\mathbf{n}_0^T \ \mathbf{n}_1^T \ \cdots \ \mathbf{n}_{L-1}^T)^T \\ \mathbf{x}_\Lambda &= (\mathbf{x}_{0,\Lambda}^T \ \mathbf{x}_{1,\Lambda}^T \ \cdots \ \mathbf{x}_{L-1,\Lambda}^T)^T \\ \Psi &= \text{blkdiag}(\Psi_{0,\Lambda}, \Psi_{1,\Lambda}, \dots, \Psi_{L-1,\Lambda}) \end{aligned}$$

$$\text{for } \Lambda = A_0, S_0, A_0/S_0, S_0/A_0, \quad (18)$$

the superscript “ $T$ ” denotes the matrix transpose operation, and  $\text{blkdiag}(\cdot)$  denotes block diagonal matrix operation. The respective dimensions of the dictionary matrices,  $\Psi_\Lambda$ , the measured data vector,  $\mathbf{z}$ , the reflectivity vectors,  $\mathbf{x}_\Lambda$ , and the noise vector  $\mathbf{n}$  are  $KL \times ML$ ,  $KL \times 1$ ,  $ML \times 1$ , and  $KL \times 1$ . Equation (17) can be expressed more compactly as

$$\mathbf{z} = \Psi \mathbf{x} + \mathbf{n}, \quad (19)$$

where  $\mathbf{x} = (\mathbf{x}_{A_0}^T \ \mathbf{x}_{S_0}^T \ \mathbf{x}_{A_0/S_0}^T \ \mathbf{x}_{S_0/A_0}^T)^T$  and  $\Psi = (\Psi_{A_0} \ \Psi_{S_0} \ \Psi_{A_0/S_0} \ \Psi_{S_0/A_0})$ , with respective dimensions  $4ML \times 1$  and  $KL \times 4ML$ . Note that the block diagonal nature of  $\Psi_\Lambda$  represents the inherent separability of the time-domain returns for each transducer–receiver pair, whereas the structure of the composite multimodal dictionary matrix  $\Psi$  indicates that no such separability of the distinct wave mode returns is assumed.

$$(\hat{\mathbf{x}})_m = \hat{x}^m = \left\| \left[ \hat{x}_{0,A_0}^m \ \cdots \ \hat{x}_{L-1,A_0}^m \ \hat{x}_{0,S_0}^m \ \cdots \ \hat{x}_{L-1,S_0}^m \ \hat{x}_{0,A_0/S_0}^m \ \cdots \ \hat{x}_{L-1,A_0/S_0}^m \ \hat{x}_{0,S_0/A_0}^m \ \cdots \ \hat{x}_{L-1,S_0/A_0}^m \right]^T \right\|_2. \quad (21)$$

### 3 Simulation Results

The effectiveness of the proposed multimodal scheme is first demonstrated by applying it to numerical data corresponding to a finite-element simulation of a plate with two crack-like defects. The first defect is chosen to be a surface crack, whereas the second defect is an internal crack. Finite element simulation is employed in lieu of real experiments, since it is

It is noted that if downsampling in the time and/or spatial domains is desired, it can be incorporated in the signal model via premultiplying  $\mathbf{z}$  by a downsampling matrix. For more details on the design of the downsampling matrix, refer to Refs. 29 and 30.

### 2.3 Group Sparse Reconstruction

Although the defect reflectivities vary from one transmitter–receiver pair to the next and from one mode to another, the defect locations remain unchanged as all transmitter–receiver pairs are inspecting the same physical scene, potentially from different viewpoints. That is, if a particular element of  $\mathbf{x}_{0,A_0}$  is nonzero, then so are the corresponding elements of  $\mathbf{x}_{l,A_0}$ ,  $\mathbf{x}_{l,S_0}$ ,  $\mathbf{x}_{l,A_0/S_0}$ , and  $\mathbf{x}_{l,S_0/A_0}$  for all  $l = 0, 1, \dots, L-1$ . In other words, the various reflectivity vectors share a common support, leading to a “group” sparsity pattern in the vector  $\mathbf{x}$  with each group extending across the four considered modes and the  $L$  transmitter–receiver pairs for each pixel location. As such, the vector  $\mathbf{x}$  can be recovered from the measurements  $\mathbf{z}$  through a mixed  $l_2/l_1$  norm optimization<sup>31–33</sup>

$$\hat{\mathbf{x}} = \arg \min_{\mathbf{x}} \frac{1}{2} \|\mathbf{z} - \Psi \mathbf{x}\|_2^2 + \lambda \|\mathbf{x}\|_{2,1}, \quad (20)$$

where  $\|\mathbf{x}\|_{2,1} = \sum_{m=0}^{M-1} \left\| \left( \hat{x}_{0,A_0}^m \ \cdots \ \hat{x}_{L-1,A_0}^m \ \hat{x}_{0,S_0}^m \ \cdots \ \hat{x}_{L-1,S_0}^m \ \hat{x}_{0,A_0/S_0}^m \ \cdots \ \hat{x}_{L-1,A_0/S_0}^m \ \hat{x}_{0,S_0/A_0}^m \ \cdots \ \hat{x}_{L-1,S_0/A_0}^m \right)^T \right\|_2$  with the superscript “ $m$ ” indicating the  $m$ 'th pixel, and  $\lambda$  is a regularization parameter. Note that the mixed norm  $\|\mathbf{x}\|_{2,1}$  is the sum (the  $l_1$ -norm) of the  $l_2$ -norms of the groups and thereby encourages occurrences of whole groups of zeros in the solution while minimizing the number of nonzero groups. Rather than solving Eq. (20) explicitly, which can be computationally expensive, greedy algorithms, such as a Block version of the Orthogonal Matching Pursuit (BOMP), can be used to recover the vector  $\mathbf{x}$  from the measurements  $\mathbf{z}$ .<sup>34</sup> BOMP relies on an iterative process to identify the support of  $\mathbf{x}$  one group at a time. The algorithm begins by initializing the residual as the measurements  $\mathbf{z}$ . At each iteration, a group is chosen that is best matched to the residual and is added to the support estimate. Candidate values of the entries of  $\mathbf{x}$  on this support are then computed using a least squares technique, and the residual is updated. This procedure is repeated until a stopping criterion (e.g., a preset iteration number also referred to as the prescribed sparsity) is satisfied. Because of the efficient manner in which this algorithm produces an accurate solution, we use BOMP for reconstruction of the ROI.

After the vector  $\hat{\mathbf{x}}$  has been recovered, a single composite representation of the ROI is obtained as<sup>33</sup>

difficult to create these defects in a real plate. Both defects are constructed such that they are symmetric with respect to the midplane of the plate; hence, these defects will scatter incident modes without spawning additional modes. The multimodal nature of the problem arises from the fact that the transmitters are assumed to simultaneously generate both fundamental Lamb modes,  $A_0$  and  $S_0$ .

### 3.1 Simulation Parameters

Simulations are performed using the Abaqus/EXPLICIT commercial finite-element analysis (FEA) software. The simulation environment consists of a 3-mm-thick aluminum plate, whose square base dimension is 600 mm. The plate is created using Abaqus “TIE” constraints to perfectly bond together two identical half-plates of size 300 mm  $\times$  600 mm  $\times$  3 mm along their longest dimension. The action of five piezoelectric transducers is simulated through an appropriate force excitation at five nodes on the surface of the plate model (see Fig. 1). This arrangement provides a total of  $L = 10$  unique transmitter–receiver combinations. The “transducer” nodes are excited via a Hanning-windowed, five-cycle burst of a 150-kHz sinusoidal signal. The 150-kHz center frequency is chosen because only  $S_0$  and  $A_0$  modes can propagate at this frequency for the considered plate thickness.

The excitation signal is introduced into the simulation as a concentrated load applied on the top and bottom surface of the plate at the transducer locations. The direction of the load is in the positive or outward normal ( $z$ -axis) direction to the plate. The time-varying amplitude,  $A(t)$ , of the load corresponds to the aforementioned five-cycle tone burst. To generate a pure  $A_0$  mode, the load on the top and bottom of the plate are both applied in the  $+z$  direction with magnitude  $\eta_A$ . The resulting force  $\Gamma(t) = \eta_A A(t)$  produces an  $A_0$  wave with normalized amplitude. Similarly, a force  $\Gamma_{\text{top/bottom}}(t) = \pm \eta_S A(t)$  is applied with constant  $\eta_S$  chosen so as to produce an  $S_0$  wave of normalized amplitude, where the signs indicates that the force is applied on the top and bottom of the plate in opposite directions along the  $z$ -axis. Using the principle of superposition, both modes are simultaneously produced when  $\Gamma_{\text{top/bottom}}(t) = (\eta_A \pm \eta_S) A(t)$  is applied at the top and bottom surfaces of the plate in the direction of the plate normal. This force is employed in the simulations herein, to ensure that symmetric and antisymmetric wave modes propagate simultaneously in the plate.

The ROI is chosen to be a 140 mm  $\times$  140 mm square area at the center of the plate (see Fig. 1). This ensures that the plate boundary is sufficiently far from the transducer and defect locations. Hence, boundary reflections are considered to be insignificant and are not included in the simulated data. The ROI is divided into a 15  $\times$  15 pixel-grid resulting in a total of  $M = 225$  pixels and the origin of the coordinate system is chosen to be at the center of the ROI. Two defects are implemented by “unTIEing” nodes such that the TIE constraint in the area of the defect does not exist. This creates discrete finite scattering boundaries at the locations of the defects, as shown in Fig. 2. The first defect, centered at  $(-34.5, 0)$  mm, has a length of 45 mm ( $x$ -direction) and a width with effective extent such that it touches the pixel locations at  $\pm 10$  mm in the  $y$ -direction. This defect is constructed as a symmetric surface crack with a depth of 0.6 mm on the top and 0.6 mm on the bottom. This type of defect will interact strongly with the incident  $A_0$  mode and weakly with the incident  $S_0$  mode. The second defect is centered at  $(67.5, 0)$  mm and is identical in length and width to the first defect. As shown in Fig. 2, it is symmetrically centered relative to the midplane of the plate such that it represents an internal crack. It spans a thickness of 1.8 mm. This type of defect has a strong interaction with the incident  $S_0$  mode, but a weak response to the incident  $A_0$  mode.

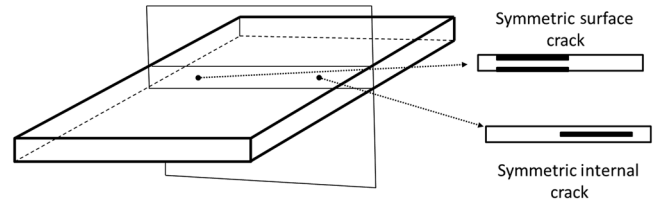


**Fig. 2** Cross-section of the plate along the plane normal to the plate, where the union of the two plate halves would be “TIEd” together except in the regions spanning the defects. Top right shows the symmetric surface crack, while bottom right depicts a symmetric internal crack.

For each transmitter–receiver pair, the received signal, acquired via Abaqus, is sampled at a rate of 1 MHz, resulting in  $K = 130$  recorded samples over a time interval of 130  $\mu$ s. As such, the measurement vector  $\mathbf{z}$  has a length of 1300. Since the symmetric nature of the implemented defects implies that no mode conversion occurs, the converted modes are excluded from the signal model in Eq. (19). Therefore, the combined reflectivity vector  $\mathbf{x} = [\mathbf{x}_{A_0}^T \ \mathbf{x}_{S_0}^T]^T$  is of length 4500, the dictionaries,  $\Psi_{A_0}$  and  $\Psi_{S_0}$  are of size 1300  $\times$  2250 each, and the composite dictionary  $\Psi = [\Psi_{A_0} \ \Psi_{S_0}]$  is of dimension 1300  $\times$  4500. The dictionaries are obtained using the analytical formulation in Sec. 2.

### 3.2 Reconstruction Results

In order to minimize mismatch errors resulting from a real-valued signal being reconstructed with a complex-valued dictionary, the Hilbert transform of the in-phase signal is utilized to create an analytic representation of the measured signal. First, using the multimodal measurement vector  $\mathbf{z}$ , single-mode-based sparse recovery is performed for the  $A_0$  and  $S_0$  modes individually. More specifically, BOMP is used to separately reconstruct the reflectivity vectors  $\mathbf{x}_{S_0}$  and  $\mathbf{x}_{A_0}$  by considering respective individual single-mode signal models  $\mathbf{z} = \Psi_{S_0} \mathbf{x}_{S_0}$  and  $\mathbf{z} = \Psi_{A_0} \mathbf{x}_{A_0}$ , with the groups extending across the various transducer pairs. The number of BOMP iterations in each case was set to 2, corresponding to the anticipated 2 defects present. Figures 3(a) and 3(b) show the single-mode results for the  $A_0$  and  $S_0$  modes, respectively. The image intensity in each figure is plotted with the maximum intensity value normalized to 0 dB. As expected, the  $A_0$  only reconstruction properly locates the surface crack, which preferentially scatters  $A_0$ , but fails to correctly localize the other defect. For the  $S_0$  only case, the reconstructed internal crack defect is in close proximity of the true location, but the other defect is missed by a relatively larger margin.

Next, the proposed multimodal approach is employed for scene reconstruction. Two iterations of BOMP are used for group sparse recovery of the multimodal reflectivity vector. However, the groups extend across both the transducer pairs and the two fundamental modes. No converted modes are considered due to the symmetric nature of the FEA modeled defects. The corresponding result is shown in Fig. 4(a), which shows that both defects have been accurately localized. For comparison, Fig. 4(b) shows the noncoherent combining of the single mode results of Fig. 3. That is, the intensities of the individual mode reconstructions are added together, i.e., group sparsity is not applied across the wave modes. This combining is clearly inferior to the proposed multimodal group sparse approach. The results presented

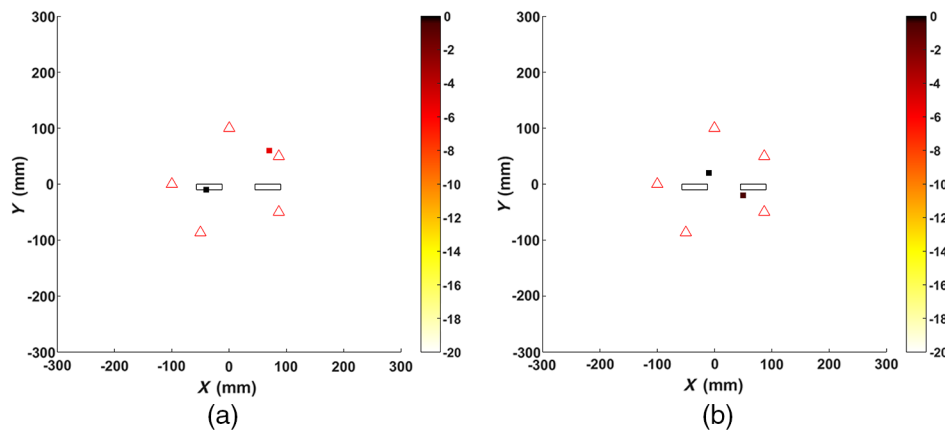


**Fig. 3** Single-mode reconstruction results with BOMP using the (a)  $A_0$  mode and (b) the  $S_0$  mode. The true defect locations are indicated by open rectangles, while the transducer locations are represented by red triangles.

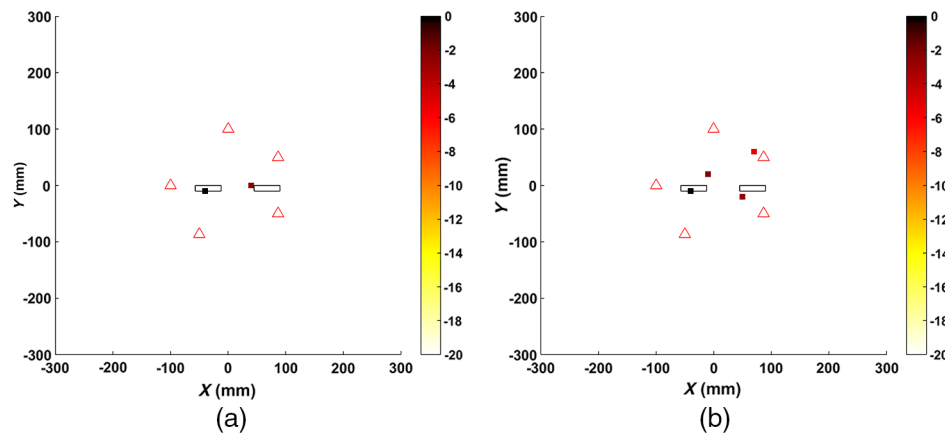


**Fig. 4** (a) Multimodal reconstruction using BOMP and (b) noncoherent combining of  $A_0$  and  $S_0$  only results. The open rectangles and the red triangles specify the true defect and transducer locations, respectively.

in Figs. 3 and 4 clearly demonstrate that the proposed multimodal approach is able to simultaneously detect defects that interact primarily with the  $S_0$  mode and those that scatter strongly the  $A_0$  mode. As it is apparent from Fig. 3, a single-mode only approach would miss one of these defects.

It is noted that BOMP, like other greedy algorithms, requires the specification of the scene sparsity for exact reconstruction. However, in practice, this information is not available *a priori* and the choice of the number of iterations is heuristic. Overspecification of the sparsity will cause measurement noise to be reconstructed in the image. The magnitude of these false reconstructions will, in general, be weaker relative to the intensities assigned to the true defects, provided that the signal-to-noise ratio (SNR) is high. Various adaptive approaches have been proposed to counter the problem of signal reconstruction without prior information of the sparsity under low SNR conditions.<sup>35,36</sup>

It is further noted that the extended nature of the crack-like defects can be incorporated as part of the reconstruction process.<sup>23,33</sup> However, since the objective of this paper is to demonstrate the offerings of multimodal imaging, the simpler point-like defect model is employed for sparse reconstruction. Nevertheless, this discrepancy between the assumed point-like defect model and the extended defect

modeled in the FEA software contributes to the reconstruction errors. Furthermore, the errors in the single-mode reconstructions, in particular, can also be attributed to the high coherence of the corresponding dictionaries (the coherence of a dictionary can be seen as the maximum correlation between any two of its columns).

### 3.3 Quantitative Performance Evaluation

In order to provide a quantitative assessment of the performance of the proposed multimodal approach, Earth movers distance (EMD) is used as a metric.<sup>37,38</sup> EMD reflects the amount of work needed to transform the reconstructed image into the ground truth image, with a value of 0 implying perfect reconstruction. In this work, a fast implementation of EMD is utilized.<sup>38</sup> The EMD corresponding to the two-defect FEA simulation is plotted versus SNR in Fig. 5 for the single-mode and multimodal approaches. SNR values in the  $[-20, 20]$  dB range with 10-dB increment are considered. In order to generate these plots, white Gaussian noise is added to the FEA measurements. A total of 100 Monte-Carlo runs are conducted for each SNR value with a different realization of noise each time, and the average EMD value is plotted. It is observed from Fig. 5 that for both single-mode

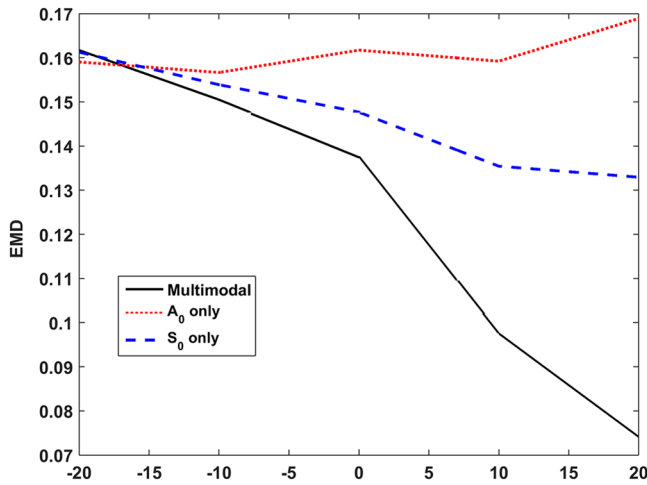


Fig. 5 EMD values for the single and multimodal approaches.

and multimodal reconstructions, the EMD tends to decrease as SNR increases. Further, the multimodal approach provides a superior reconstruction as manifested in a significantly lower EMD value when compared to the single-mode approaches for SNR values greater than 0 dB. These results quantify and validate the superior performance of the proposed multimodal approach over the single-mode only reconstructions.

## 4 Experimental Results

In this section, the proposed multimodal approach is applied to real data measurements from an aluminum plate with asymmetric point-like defects. Such defects produce both scattered and spawned modes corresponding to the propagating  $A_0$  and  $S_0$  modes.

### 4.1 Experimental Setup

We utilize a sparsely distributed transducer array of five lead zirconate titanate (PZT) piezoelectric transducers attached to a 1.22-m square and 3.12-mm-thick aluminum plate. The transducers, manufactured by APC International, are 0.22 mm thick with 10 mm diameter. The transducers are arranged in a circle of radius 250 mm at the locations shown in Fig. 6. A pitch-catch mode was employed resulting in a total of  $L = 10$  distinct transmitter-receiver pairs.

The transducers are excited via a Hanning-windowed, five-cycle burst of a 150-kHz sinusoidal signal. The 150-kHz center frequency permits only  $S_0$  and  $A_0$  modes to propagate in the material. The group velocities for the  $S_0$  and  $A_0$  at the frequency-thickness of 0.234 MHz-mm are 5338 and 1827 m/s, respectively, with a packet width of 33.4  $\mu$ s. The combined packet width and velocity difference permits sufficient temporal separation of the arriving wave packets for the two fundamental modes, while the converted modes merge together into a single third packet. National Instruments (NI) PXI 5142 Arbitrary Waveform Generator is used for signal generation, in conjunction with a Krohn-Hite Model 7500 Amplifier, whose gain is set to 40 dB so as to ensure a strong incident wave. Received data measurements are compiled and averaged over 5000 collections in LabView via an NI PXI 5105 Digitizer operating at a sampling rate of 1 MHz. Both the PXI 5142 and 5105 are housed in an NI PXI 8108 Embedded Controller.

Defects are introduced by adhering steel rods to the plate using a simple two-part epoxy. The rods have a diameter of 12.7 mm and are of two different heights: 50 and 57.5 mm. The rods are glued on the top surface of the plate, with the 50 mm tall rod located at (160, 160) mm and the 57.5 mm tall rod attached at (340, 340) mm, as shown in Fig. 6(a). The origin of the coordinate system is located in the lower left hand corner in Fig. 6(a). This defect configuration creates a realistic scenario of asymmetric defects. The ROI is a  $400 \times 400$  mm square centered at (250, 250) mm and is divided into  $31 \times 31$  grid points resulting in  $M = 961$  pixels. The plate temperature is monitored using a J-type thermocouple. The thermocouple is glued to the plate with thermal epoxy just outside the ROI, and its voltage is recorded with an NI 9211 Thermocouple Input. LabView converts this continuous feed to temperature and displays it in real time. Due to the dependence of the signal amplitude on temperature, this step is necessary to ensure a clean residual using optimal baseline subtraction.<sup>39</sup>

### 4.2 Reconstruction Results

The measurement system only captures the in-phase components of the received signals. Therefore, the Hilbert transform of the in-phase signal is again utilized to create an analytic signal representation of the measured signal. The complex-valued signals corresponding to each transmitter-receiver pair are time-windowed retaining the returns up to 340  $\mu$ s corresponding to the interval of interest, resulting in  $K = 340$  samples. Thus, the measurement vector  $\mathbf{z}$  is of dimension  $3400 \times 1$ .

As described earlier, asymmetric defects cause mode conversion in addition to scattering of the incident modes. Therefore, unlike the FEA simulation, which dealt with the scattered  $S_0$  and  $A_0$  modes only, the converted mode components are included in the signal model and reconstruction approach in this case. As such, the combined reflectivity vector  $\mathbf{x}$  is of length 38,440, and the composite dictionary  $\Psi$  is of dimension  $3400 \times 38,440$ . The BOMP-based multimodal and single-mode only reconstruction results are shown in Fig. 7. Black circles and red triangles indicate the actual defect and transducer locations, respectively. The number of BOMP iterations is set to 2 for each reconstruction. The multimodal result accounting for mode conversion in Fig. 7(c) reconstructs the defect at (160, 160) mm with a slightly biased location, while the other defect has been accurately localized. The  $A_0$  only reconstruction in Fig. 7(a) provides comparable performance to the multimodal reconstruction in terms of location accuracy, but assigns its selections a much weaker magnitude. On the other hand, the  $S_0$  only result in Fig. 7(b) fails to localize both defects, which is attributed primarily to the relatively weak  $S_0$  mode at 150 kHz compared to the  $A_0$  mode. For comparison, Fig. 7(d) shows the noncoherent combining of the  $A_0$  only and the  $S_0$  only reconstructions. Although this simple combining of individual mode reconstructions is able to localize the defects, it is more cluttered compared to the group sparsity multimodal reconstruction. Figure 7(e) provides the multimodal result when mode conversion is ignored. As it is evident, ignoring this phenomenon results in an image identical to Fig. 7(a) where only the  $A_0$  mode is considered. The two localizations are accurate; however, the selections are assigned much weaker magnitudes relative to the

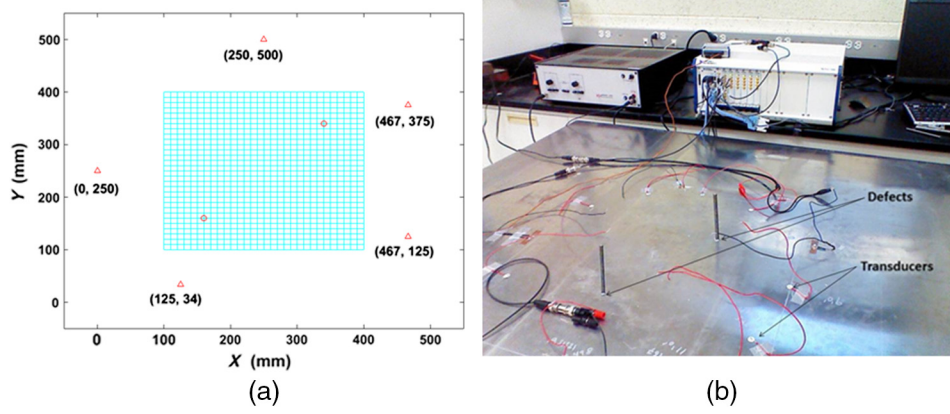


**Fig. 6** Experimental setup. (a) Schematic showing the pixel grid in cyan, with PZT transducer location indicated by red triangles and defects marked by red circles at (160, 160) mm and (340, 340) mm. (b) Actual setup.

multimodal results accounting for mode conversion as seen in Fig. 7(c).

To quantify the performance quantitatively, the EMD is computed for the four reconstructions after each image has been normalized to have a maximum intensity of

0 dB. The  $A_0$  only and  $S_0$  only reconstructions have respective EMD values of 0.0015 and 0.0461. The multimodal result that ignored mode conversion matches the  $A_0$  only result with an EMD value of 0.0015. The noncoherent combining of the single mode only results has an EMD of

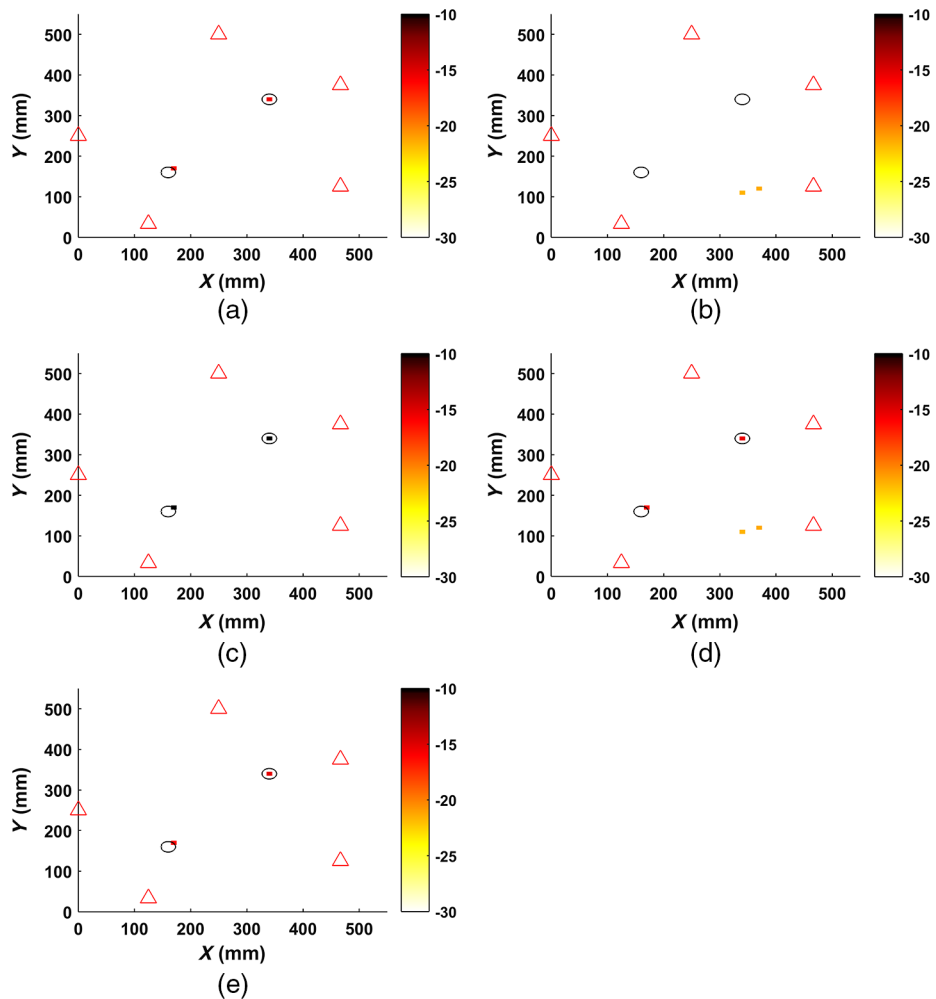


**Fig. 7** Sparse reconstructions for the two-defect experiment. (a)  $A_0$  only, (b)  $S_0$  only, (c) multimodal accounting for mode conversion, (d) noncoherent combining of  $A_0$  and  $S_0$  only results, and (e) multimodal ignoring mode conversion.

0.0462, while the EMD for the proposed multimodal approach is determined to be 0.00091. These values confirm the performance enhancement offered by the multimodal approach.

## 5 Conclusion

In this paper, a sparse reconstruction approach is proposed for detecting defects in thin plates, which exploits the multimodal nature of Lamb waves and imposes a block structure across the modes and the transducer pairs within the modes. Model-based dictionaries, which account for the associated dispersion and attenuation through the medium, are constructed for the directly scattered fundamental wave modes as well as the defect-spawned converted modes. Results based on simulated data from an FEA model of scattering by two symmetric crack-like defects in a thin aluminum plate were used to validate the dictionary constructions and for performance evaluation of the proposed multimodal scheme. These results exposed the shortcomings of single-mode only reconstructions and highlighted the superior performance of the proposed multimodal approach. The effectiveness of the multimodal approach was further demonstrated using experimental data collected from a thin aluminum plate with two point-like defects. The corresponding multimodal reconstruction was accurate to within one pixel, which is well within the tolerance of what is acceptable in real world applications.

## Acknowledgments

This work was supported by the National Science Foundation under Grant No. IIP-0917690.

## References

- S. S. Kessler, S. M. Spearing, and C. Soutis, "Damage detection in composite materials using Lamb wave methods," *Smart Mater. Struct.* **11**(2), 269–278 (2002).
- A. Raghavan and C. E. S. Cesnik, "A review of guided wave structural health monitoring," *Shock Vib. Dig.* **39**(2), 91–114 (2007).
- V. Giurgiutiu and G. Santoni-Bottai, "Structural health monitoring of composite structures with piezoelectric wafer active sensors," *Am. Inst. Aeronaut. Astronaut. J.* **49**(3), 565–581 (2011).
- S. Santhanam and R. Demirli, "Reflection and transmission of fundamental Lamb wave modes obliquely incident on a crack in a plate," in *Proc. IEEE Int. Ultrasonics Symp.*, pp. 2690–2693 (2012).
- R. J. Ditchburn, S. K. Burke, and C. M. Scala, "NDT of welds: state of the art," *NDT&E Int.* **29**(2), 111–117 (1996).
- M. J. S. Lowe, D. N. Alleyne, and P. Cawley, "Defect detection in pipes using guided waves," *Ultrasonics* **36**(1–5), 147–154 (1998).
- X. Zhao et al., "Active health monitoring of an aircraft wing with embedded piezoelectric sensor/actuator network: I. Defect detection, localization and growth monitoring," *Smart Mater. Struct.* **16**(4), 1208–1217 (2007).
- X. Li, Z. Yang, and X. Chen, "Quantitative damage detection and sparse sensor array optimization of carbon fiber reinforced resin composite laminates for wind turbine blade structural health monitoring," *Sensors* **14**(4), 7312–7331 (2014).
- H. Lamb, "On waves in an elastic plate," *Proc. R. Soc. London Ser. A* **93**, 114–128 (1917).
- D. C. Worlton, "Experimental confirmation of Lamb waves at megacycle frequencies," *J. Appl. Phys.* **32**, 967–971 (1961).
- J. Rose, *Ultrasonic Waves in Solid Media*, Cambridge University Press, Cambridge (1999).
- C. Ramadas et al., "Interaction of the primary antisymmetric Lamb mode ( $A_0$ ) with the symmetric delaminations: numerical and experimental studies," *Smart Mater. Struct.* **18**(8), 085011 (2009).
- P. Tua, S. Quek, and Q. Wang, "Detection of cracks in plates using piezo-actuated Lamb waves," *Smart Mater. Struct.* **13**(4), 643–660 (2004).
- D. N. Alleyne and P. Cawley, "The interaction of Lamb waves with defects," *IEEE Trans. Ultrason. Ferroelect. Freq. Control* **39**(3), 381–397 (1992).
- N. Guo and P. Cawley, "The interaction of Lamb waves with delaminations in composite laminates," *J. Acoust. Soc. Am.* **94**(4), 2240–2246 (1993).
- R. M. Levine and J. E. Michaels, "Model-based imaging of damage with Lamb waves via sparse reconstruction," *J. Acoust. Soc. Am.* **133**(3), 1525–1534 (2013).
- S. Santhanam and R. Demirli, "Reflection of Lamb waves obliquely incident on the free edge of a plate," *Ultrasonics* **53**(1), 271–282 (2013).
- C. Ng and M. Veidt, "Scattering of the fundamental antisymmetric Lamb wave at delaminations in composite laminates," *J. Acoust. Soc. Am.* **129**(3), 1288–1296 (2011).
- C. H. Wang, J. T. Rose, and F. K. Chang, "A synthetic time-reversal imaging method for structural health monitoring," *Smart Mater. Struct.* **13**(2), 415–423 (2004).
- D. H. Johnson and D. E. Dudgeon, *Array Signal Processing: Concepts and Techniques*, Prentice Hall, New Jersey (1993).
- J. Hall and J. Michaels, "Minimum variance ultrasonic imaging applied to an in situ sparse guided wave array," *IEEE Trans. Ultrason., Ferroelect., Freq. Control* **57**(10), 2311–2323 (2010).
- R. M. Levine and J. E. Michaels, "Block-sparse reconstruction and imaging for lamb wave structural health monitoring," *IEEE Trans. Ultrason. Ferroelect. Freq. Control* **61**(6), 1006–1015 (2014).
- Q. Wu et al., "Structure health monitoring exploiting MIMO ultrasonic sensing and group sparse Bayesian learning," in *Proc. Asilomar Conf. Signals, Systems, and Computers*, pp. 1162–1166 (2014).
- F. Foroozan and S. Shahbazpanahi, "MUSIC-based array imaging in multi-modal ultrasonic non-destructive testing," in *Proc. IEEE 7th Sensor Array and Multi-channel Signal Processing Workshop*, pp. 529–532 (2012).
- J. B. Harley and J. M. F. Moura, "Data-driven matched field processing for Lamb wave structural health monitoring," *J. Acoust. Soc. Am.* **135**(3), 1231–1244 (2014).
- S. Hamidi and S. ShahbazPanahi, "Sparse signal recovery based imaging in the presence of mode conversion with application to non-destructive testing," *IEEE Trans. Signal Process.* **64**(5), 1352–1364 (2016).
- A. Golato et al., "Multimodal sparse reconstruction in Lamb wave-based structural health monitoring," *Proc. SPIE* **9109**, 91090P (2014).
- A. Golato et al., "Multimodal exploitation and sparse reconstruction for guided-wave structural health monitoring," *Proc. SPIE* **9484**, 94840L (2015).
- A. C. Gurbuz, J. H. McClellan, and W. R. Scott Jr., "Compressive sensing for subsurface imaging using ground penetrating radar," *Signal Process.* **89**(10), 1959–1972 (2009).
- J. Qian, F. Ahmad, and M. G. Amin, "Joint localization of stationary and moving targets behind walls using sparse scene recovery," *J. Electron. Imaging* **22**(2), 021002 (2013).
- W. Deng, W. Yin, and Y. Zhang, "Group sparse optimization by alternating direction method," *Department of Computational and Applied Mathematics*, Rice University, Technical Report TR11-06 (2011).
- M. Yuan and Y. Lin, "Model selection and estimation in regression with grouped variables," *J. R. Stat. Soc. B* **68**(1), 49–67 (2006).
- M. Leigsnering et al., "Multipath exploitation in through-the-wall radar imaging using sparse reconstruction," *IEEE Trans. Aerosp. Electron. Syst.* **50**(2), 920–939 (2014).
- Y. C. Eldar, P. Kuppinger, and H. Bolckei, "Block-sparse signals: uncertainty relations and efficient recovery," *IEEE Trans. Signal Process.* **58**(6), 3042–3054 (2010).
- H. Sun et al., "Compressive autonomous sensing (CAsE) for wideband spectrum sensing," in *Proc. IEEE Int. Communications Conf.*, pp. 4442–4446 (2012).
- T. T. Do et al., "Sparsity adaptive matching pursuit algorithm for practical compressed sensing," in *Proc. 42nd Asilomar Conf. on Signals, Systems and Computers*, pp. 581–587 (2008).
- Y. Rubner, "Perceptual metrics for image database navigation," PhD Thesis, Stanford University (1999).
- O. Pele and M. Werman, "Fast and robust earth mover's distances," in *Proc. IEEE 12th Int. Conf. Computer Vision*, pp. 460–467 (2009).
- G. Konstantinidis, B. W. Drinkwater, and P. D. Wilcox, "The temperature stability of guided wave structural health monitoring systems," *Smart Mater. Struct.* **15**(4), 967–976 (2006).

**Andrew Golato** received his BS degree in physics from Haverford College in 2012 with a biophysics thesis on fluid dynamics. He received his MS degree in mechanical engineering in 2014 from Villanova University. He is currently a PhD candidate at Villanova University conducting research on sparsity-based guided-wave structural health monitoring.

**Sridhar Santhanam** is a professor in the Mechanical Engineering Department at Villanova University. He received his bachelor's degree in mechanical engineering from the Indian Institute of Technology, Chennai, in 1984, his master's degree in 1986 and his

PhD in 1989 in mechanical engineering from Arizona State University in Tempe, Arizona. His research interests are in the areas of modeling and characterization of materials and structural health monitoring.

**Fauzia Ahmad** received her PhD in electrical engineering from the University of Pennsylvania in 1997. She is a research professor with the Center for Advanced Communications at Villanova University. She has published 200+ journal and conference papers on statistical signal processing, radar imaging, ultrasound imaging, and compressive sensing. She is an associate editor of JEI, chair of the SPIE

Compressive Sensing Conference, and a senior member of IEEE and SPIE.

**Moeness G. Amin** is the director of the Center for Advanced Communications at Villanova University, Pennsylvania. He is a fellow of IEEE, SPIE, Institute of Engineering and Technology, and the European Association for Signal Processing. He is a recipient of the 2016 Humboldt Prize, 2015 IEEE Warren D. White Award for Excellence in Radar Engineering, and 2014 IEEE Signal Processing Society Technical Achievement Award. He has over 700 publications in signal processing theory and applications.